Observational inferences of lateral eddy diffusivity in the halocline of the Beaufort Gyre

Gianluca Meneghello[1], John Marshall[1], Sylvia T. Cole[2], and Mary-Louise Timmermans[3]

[1]Department of Earth, Atmospheric and Planetary Sciences, Massachusetts Institute of Technology, Cambridge, Massachusetts, USA
[2]Woods Hole Oceanographic Institution, Woods Hole, Massachusetts, USA
[3]Department of Geology and Geophysics, Yale University, New Haven, Connecticut, USA,

Key Points:

- Eddy diffusivity in the Beaufort Gyre (BG) ranges from 100-500 $m^2\,s^{-1}$ near the surface, decaying rapidly with depth across the halocline
- Eddy-induced upwelling largely compensates downward Ekman pumping in the BG
- Lateral eddy diffusivity plays a zero-order role in the freshwater budget of the BG

Corresponding author: Gianluca Meneghello, gianluca.meneghello@gmail.com

Abstract

Using Ekman pumping rates mediated by sea-ice in the Arctic Ocean's Beaufort Gyre (BG), the magnitude of lateral eddy diffusivities required to balance downward pumping is inferred. In this limit — that of vanishing residual-mean circulation — eddy-induced upwelling exactly balances downward pumping. The implied eddy diffusivity varies spatially and decays with depth, with values of 50-400 $\mathrm{m^2\,s^{-1}}$. Eddy diffusivity estimated using mixing length theory applied to BG mooring data exhibits a similar decay with depth and range of values from $100\,\mathrm{m^2\,s^{-1}}$ to more than $600\,\mathrm{m^2\,s^{-1}}$. We conclude that eddy diffusivities in the BG are likely large enough to balance downward Ekman pumping, arresting the deepening of the gyre and suggesting that eddies play a zero-order role in buoyancy and freshwater budgets of the BG.

1 Introduction

The Arctic Ocean's Beaufort Gyre, centered in the Canada Basin, is characterized by a strong halocline stratification with relatively fresh surface waters overlying saltier (and warmer) waters of Atlantic Ocean origin. The halocline stratification inhibits the vertical flux of ocean heat to the overlying sea-ice cover. The halocline is deepened by Ekman pumping associated with a persistent but highly variable Arctic high pressure system [*Proshutinsky and Johnson*, 1997; *Proshutinsky et al.*, 2009, 2015]. This creates the anticyclonic Beaufort Gyre (BG) in which salinity surfaces bow downwards creating a bowl of freshwater, the main reservoir of freshwater in the Arctic.

Due to the store of available potential energy associated with its tilted isopycnal surfaces, the BG is highly susceptible to baroclinic instability and indeed a ubiquitous mesoscale eddy field is a notable feature of observations [*Manley and Hunkins*, 1985; *Timmermans et al.*, 2008; *Zhao et al.*, 2014, 2016].

Through idealized modeling studies, the mesoscale eddy field, which includes coherent eddies (of order 10 km in diameter) as well as fluctuations on order 100 km scales [*Nurser and Bacon*, 2014], has been implicated in playing a key role in equilibrating the freshwater budget of the BG [*Manucharyan et al.*, 2016; *Manucharyan and Spall*, 2016]. However it is difficult to quantify the importance of the eddy field in the large-scale dynamics directly from observations. This quantification and an assessment of the contribution of the eddy induced circulation to the dynamics of the BG are the main goals of the present study.

Here we apply a residual-mean framework to examine whether observations in the BG are consistent with eddies playing a leading order role in the dynamics and transport. The residual-mean circulation is the sum of the mean flow (i.e., the Eulerian-mean circulation) plus transport by eddies (i.e., the bolus transport). This decomposition has proven effective, for example, for understanding Southern Ocean dynamics [*Danabasoglu et al.*, 1996; *Marshall and Radko*, 2003; *Marshall and Speer*, 2012]. In the Southern Ocean the wind-driven Deacon Cell is largely balanced by a mesoscale eddy-induced overturning cell, and the residual-mean circulation vanishes.

We test the hypothesis that wind driving of the large-scale anticyclonic BG circulation is balanced by eddy fluxes (bolus fluxes). In this balance (shown schematically by black arrows in Figure 1), the residual-mean circulation is zero and a relationship may be derived between lateral eddy diffusivity K_D, surface-ocean stress, and isopycnal slopes of the large-scale gyre. Observations of the latter two then allow for estimates of K_D. We go on to compare the spatial patterns and magnitudes of the diffusivities to those computed directly using mixing length theory applied to timeseries from four moorings deployed in the BG.

The paper is set out as follows. In Section 2 we describe BG observations and wind forcing used in the analysis. In Section 3, guided by residual-mean theory, we infer BG halocline eddy diffusivities required to bring the BG residual flow to zero. In Section 4 we show

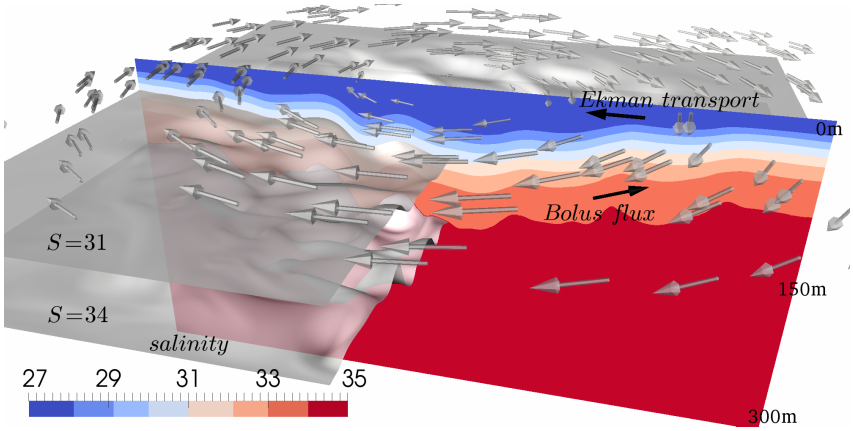

Figure 1. Schematic of the hydrography and circulation of the Beaufort Gyre, fresh (blue) at the surface and salty (red) below. The grey arrows represent the anticyclonic forcing of the gyre by the prevailing winds. The top black arrow represents freshwater being gathered towards the center of the gyre by wind-driven Ekman transport, the convergence of which pumps down into the center of the gyre. This causes salinity surfaces to bow downward into the interior, deep in the center and shallow on the periphery of the gyre. The baroclinic instability of the gyre has the tendency to flatten salinity surfaces and results in an eddy bolus flux (black arrow at depth) of freshwater directed outward from the center, offsetting the inward flux at the surface.

that these estimates are similar to those deduced from mooring data. In Section 5 we conclude with a discussion of the implications of our study.

2 Observed structure of the Beaufort Gyre and wind forcing

To estimate the air-ocean and ice-ocean stress $\boldsymbol{\tau}$ and Ekman pumping $w_{Ek} = \frac{\nabla\times\boldsymbol{\tau}}{\rho_0 f_0}$, we follow the approach of *Yang* [2006, 2009]. We use $\rho_0 = 1027.5\,\mathrm{kg\,m^{-3}}$ as a reference density for water and $f_0 = 1.46\times10^{-4}\,\mathrm{s^{-1}}$ as the Coriolis parameter. The mean surface stress $\boldsymbol{\tau}$ is computed by averaging daily surface stresses, obtained as a combination of ice-ocean and air-ocean surface stresses, each estimated using a quadratic drag law with fixed drag coefficients ($C_{Dice} = 0.0055$, $C_{Dair} = 0.00125$), and weighted by the observed local ice concentration α:

$$\boldsymbol{\tau} = \alpha \underbrace{\rho_0 C_{Dice}\,|\boldsymbol{u}_{rel}|\,(\boldsymbol{u}_{rel})}_{\boldsymbol{\tau}_{ice}} + (1-\alpha)\underbrace{\rho_{air} C_{Dair}\,|\boldsymbol{u}_{air}|\,(\boldsymbol{u}_{air})}_{\boldsymbol{\tau}_{air}}, \tag{1}$$

where $\boldsymbol{u}_{rel} = \boldsymbol{u}_{ice} - (\boldsymbol{u}_{geo} + \boldsymbol{u}_{Ek})$ is the relative velocity between the ice and ocean. We choose to use a reference velocity $\boldsymbol{u}_{geo} + \boldsymbol{u}_{Ek}$, representing the ocean velocity near the ice surface. Shallow and deeper reference levels can be used [*Lu et al.*, 2011]. Sensitivity to the choice of the drag coefficient's value is discussed in §3. The air density is taken as $\rho_{air} = 1.25\,\mathrm{kg\,m^{-3}}$.

To evaluate equation (1) we combine four datasets: (i) sea ice concentration α from Nimbus-7 SMMR and DMSP SSM/I-SSMIS Passive Microwave Data Version 1 [*Cavalieri et al.*, 1996]; (ii) sea ice velocity $\boldsymbol{u}_{ice}$ from the Polar Pathfinder Daily 25 km EASE-Grid Sea Ice Motion Vectors, Version 3 [*Tschudi et al.*, 2016]; (iii) surface geostrophic currents $\boldsymbol{u}_{geo}$ computed from Dynamic Ocean Topography [*Armitage et al.*, 2016, 2017] and (iv) 10 m wind $\boldsymbol{u}_{air}$ from the NCEP-NCAR Reanalysis 1 [*Kalnay et al.*, 1996]. The 2003-2012 tem-

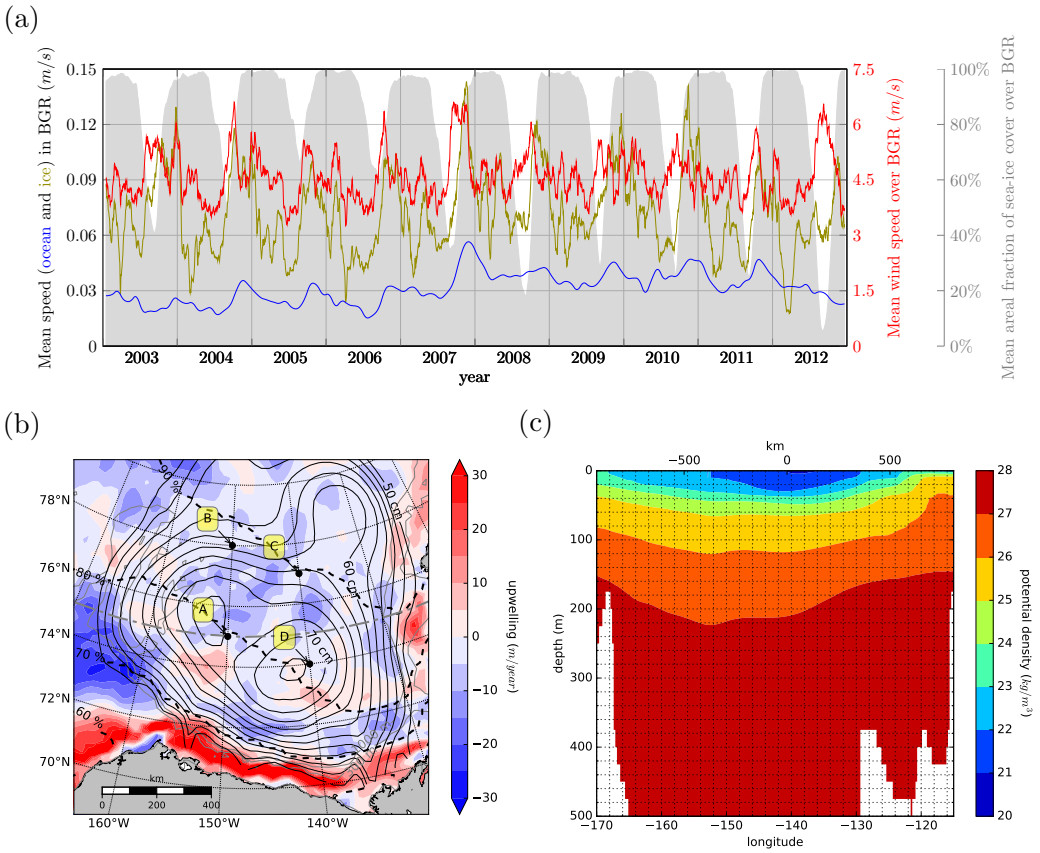

Figure 2. (a) Thirty-day running mean of sea-ice speed (green), surface geostrophic current speed (blue) and 10 m wind speed (red) over the Beaufort Gyre Region, delimited by 70.5°N-80.5°N and 170°W-130°W and including only locations with depths greater than 300 m [*Proshutinsky et al.*, 2009]. The gray shading represents mean areal fraction of sea-ice cover. The white annual downward spikes correspond to the summertime with progressively less ice cover over time, particularly in 2012. (b) The 2003-2012 climatology of Ekman pumping w_{Ek} (color) and geopotential height D computed from the 2005-2012 World Ocean Atlas (WOA) climatology (black contours, see §3); the location of the four Beaufort Gyre Observing System moorings (named A, B, C and D) are marked by black dots. Thick dashed lines show mean ice concentration. (c) hydrographic section of potential density (referenced to the surface) at 75°N (see gray dash-dotted line in panel (b)), computed from the WOA climatology.

poral variability of these four variables (mean values over the Beaufort Gyre) is summarized in Figure 2a.

Our estimate of the surface ocean current $\boldsymbol{u}_{geo} + \boldsymbol{u}_{Ek}$ differs from *Yang* [2006, 2009], however, in two key ways. First, we use the Ekman velocity at the surface (rotated 45° to the right of the surface stress) in place of the mean Ekman transport velocity (90° from the surface stress), thus $\boldsymbol{u}_{Ek} = \boldsymbol{\tau} \frac{\sqrt{2} e^{-i\frac{\pi}{4}}}{f_0 \rho_0 D_e}$, with $D_e = 20\,\mathrm{m}$ [*Yang*, 2006]. Because the Ekman velocity and the surface stress depend on each other, equation (1) is solved iteratively. Second, and more importantly, we include the surface geostrophic current $\boldsymbol{u}_{geo}$ inferred from dynamic ocean topography [*Armitage et al.*, 2016, 2017]. Similar results can be obtained using geopotential height to estimate $\boldsymbol{u}_{geo}$ [*McPhee*, 2013]. The geostrophic current speed approximately doubled after 2007 (Figure 2a, blue line), and we find that its inclusion has a non-negligible influence on Ekman pumping rates.

The 2003-2012 average Ekman pumping field inferred from observations (Figure 2b, color) depends on the prevailing winds and basin geometry, the distribution, drift speed and concentration of sea ice, and the strength of surface currents. We infer average downwelling rates of order $5\,\mathrm{m\,yr^{-1}}$ within the BG region, but there is considerable spatial structure. Strong upwelling speeds, in excess of $30\,\mathrm{m\,yr^{-1}}$, can be seen in the coastal areas south of the 300 m bathymetric contour. Northwards of this downwelling rates reach $20\,\mathrm{m\,yr^{-1}}$ corresponding to a mean sea-ice concentration between 65% and 75%. For larger mean ice concentration, the BG Region is characterized by lower downwelling rates of order $5\,\mathrm{m\,yr^{-1}}$, with localized patches of upwelling of maximum $10\,\mathrm{m\,yr^{-1}}$ around 74°N. Note however that our computations of eddy diffusivity described below depend on integrals over closed geostrophic contours and so do not depend on many of these details.

We remark that, as a consequence of the inclusion of the surface geostrophic current, our Ekman pumping field differs considerably in both intensity and spatial structure from previous results, as can be deduced by comparing Figure 2b with the results of *Yang* [2006, 2009] or *McPhee* [2013]. A more detailed discussion is provided by [Meneghello, G., J. Marshall, M. L. Timmermans, and J. Scott (2017), Observations of seasonal upwelling and downwelling in the Beaufort Sea mediated by sea ice, *Journal of Physical Oceanography*, in revision].

The hydrographic structure of the BG, based on the quarter-degree resolution 2005-2012 World Ocean Atlas Climatology [*Locarnini et al.*, 2013; *Zweng et al.*, 2013], is summarized by contours of geopotential height

$$D = \frac{1}{g} \int_0^{p_0} \left[\rho^{-1}(S,T,p) - \rho^{-1}(35,0,p) \right] dp, \tag{2}$$

where ρ^{-1} is the specific volume and $p_0 = 400\,\mathrm{dbar}$ (Figure 2b), and by a section of potential density across 75°N (Figure 2c). Potential density increases rapidly from $1022\,\mathrm{kg\,m^{-3}}$ to $1027\,\mathrm{kg\,m^{-3}}$ over the halocine in the top 300 m to join the very weakly stratified waters below. As expected from the pattern of Ekman pumping being imposed by the wind from above, isopycnals are deeper in the middle of the BG, with slopes of the order of 50 m over 500 km or less. This hydrographic structure supports, through thermal wind, the large-scale anticyclonic circulation of the gyre and is essential to our estimates of the eddy diffusivity required to balance the effect of the Ekman pumping, as outlined in the next section.

3 Eddy diffusivities in the limit of vanishing Residual Circulation

Adopting a residual mean theory framework [*Andrews and McIntyre*, 1976; *Marshall and Radko*, 2003; *Plumb and Ferrari*, 2005], we now use the observations of Ekman pumping and isopycnal slopes presented in section 2 to infer the magnitude of the eddy diffusivities required to bring the residual circulation in the halocine of the BG to zero. This is the limiting case analogous to the 'vanishing of the Deacon Cell' in the literature on Southern Ocean dynamics reviewed by Marshall and Speer (2012).

We integrate azimuthally along geopotential height contours shown in Figure 2b to represent the overturning circulation in the (r, z) plane by a streamfunction: $(v_r, w) = \left(-\frac{\partial \Psi}{\partial z}, \frac{\partial \Psi}{\partial r}\right)$, where r is a radial coordinate. In the assumed adiabatic interior of the halocline, we consider the limit case that the streamfunction describing the residual-mean circulation is vanishingly small:

$$\Psi_{res} = \overline{\Psi} + \Psi^* = 0, \tag{3}$$

where the Eulerian-mean streamfunction is given by the Ekman transport, $\overline{\Psi} = \overline{\tau}/(\rho_0 f_0)$, and the eddy-induced streamfunction is given by $\Psi^* = \overline{v_r' b'}/\overline{b}_z$, where $\overline{v_r' b'}$ is the radial eddy buoyancy flux and $\overline{b}_z$ is the vertical stratification. Overbars denote time and along-geopotential-height-contour averages. We are computing, then, the limit case in which bolus transport by eddies are sufficiently strong to exactly balance the Eulerian-mean flow set up by the wind.

As is conventional (see Gent and McWilliams, 1991) we characterise the efficiency of eddy transport by an eddy diffusivity and write, $\overline{v_r' b'} = -K_D \overline{b}_r$, and so $\Psi^* = -K_D \overline{b}_r/\overline{b}_z$. Adopting this closure as our definition of diffusivity, Eq.(3) provides a relationship between the wind stress $\overline{\tau}$, the mean buoyancy variations $\overline{b}_r$ and $\overline{b}_z$, and the eddy diffusivity K_D

$$K_D = \frac{1}{\rho_0 f_0} \frac{\overline{\tau}}{\overline{s}} \quad \text{where} \quad \overline{s} = -\frac{\overline{b}_r}{\overline{b}_z} = \frac{\partial \overline{h}}{\partial r}. \tag{4}$$

Here h is the depth of the isopycnal, r is the radial coordinate and $\overline{s}$ the slope of the isopycnal of the time and azimuthally averaged density field. For computational convenience, rather than integrating along geopotential height contours, we use the divergence and Stokes theorems to rewrite (4) as

$$K_D = \frac{1}{\rho_0 f_0} \frac{\int \nabla \times \tau \; dA}{\int \nabla^2 h \; dA}, \tag{5}$$

where the integrals are performed over the area circumscribed by a geopotential height contour and limited to regions with depth greater than 300 m, and τ and h are averaged only in time. The integrated Ekman pumping (in $\mathrm{m^3\ s^{-1}}$) and thickness flux (m), i.e. the numerator and denominator of (5) respectively, are plotted in Figure 3a for different density levels.

The estimated eddy diffusivity, ranging from $50\,\mathrm{m^2\ s^{-1}}$ to $400\,\mathrm{m^2\ s^{-1}}$, is plotted as a function of geopotential height and density in Figure 3b. We observe a strong dependence on the density level and on the geopotential height contour: higher values of eddy diffusivity are concentrated in the top 100 m from the surface (lighter than $26\,\mathrm{kg\,m^{-3}}$, see also Figure 2c) and close to the 65 cm geopotential height contour, and decay by a factor of four at greater depth and towards the center of the gyre. White areas in Figure 3b correspond to outcropping isopycnals above $25\,\mathrm{kg\,m^{-3}}$ and/or to the presence of land in at least one point along the dynamic height contour below that.

We remark that uncertainty in the evaluation of the numerator and denominator of (4) is large. There are errors in our estimates of stress due to uncertainties in Ekman layer thickness D_e, the drag coefficients C_{Dice} and C_{Dair} as well as in the accuracy of the estimated ice, wind and ocean surface velocities. As an example, decreasing (increasing) the Ekman layer thickness from 20 m [*Yang*, 2006] to 10 m (40 m) [*Cole et al.*, 2017] results in a decrease (increase) of the estimated eddy diffusivity by approximately 20%. Similarly, there are uncertainties in the ice-ocean drag coefficient C_{Dice}, which can vary between 0.001 and 0.01 depending on ice roughness, concentration and many other factors [*Lu et al.*, 2011; *Cole et al.*, 2017]. A possibly even larger source of uncertainty is associated with the wind, ice and ocean velocities used in (1). Before we go on we should note that if the mean Ekman pumping over the region were $10\,\mathrm{m\,yr^{-1}}$ instead of $5\,\mathrm{m\,yr^{-1}}$, the eddy diffusivity required to bring the residual flow to zero would be doubled.

The values of K_D shown in Figure 3 are those required to exactly balance Ekman processes. How do eddy diffusivities inferred from observations compare with those inferred by

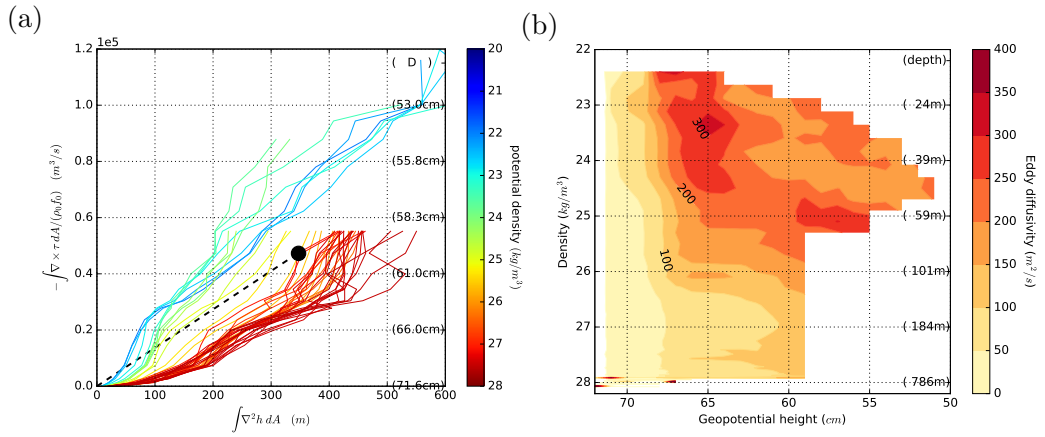

Figure 3. (a) Integrated Ekman pumping (in $m^3\ s^{-1}$) plotted against the integrated $\nabla^2 h$ (in m) at different density levels as indicated by color. The resulting eddy diffusivity K_D can be readily obtained as the ratio of the two values; for the point marked with a black dot, this is equivalent to the slope of the dashed line (in $m^2\ s^{-1}$). (b) Eddy diffusivity K_D as a function of density and geopotential height contour; the depth in parenthesis is the mean depth of the isopycnal.

assuming zero residual flow? To explore we now estimate lateral diffusivity using an entirely different method making use of hydrographic and current meter data.

4 Estimates of eddy diffusivities from mooring data

Horizontal eddy diffusivity is estimated from temperature, salinity and velocity profiles obtained from four Beaufort Gyre Observing System (BGOS) moorings, whose position are shown in Figure 2b.

Each mooring provides a pair of profiles spanning ≈50 m to 2000 m depth every 54 hours. Each pair of profiles is separated by 6 hours in time so that averaging minimizes the influence of near-inertial motions that have an approximately 12 hour period. Processed data have a 2 m vertical resolution. Data are utilized over August 2003 to August 2012, with each mooring having some years in which data were not returned (e.g., mooring A: July 2006 – Aug 2007 and July 2008 – September 2009). The record at mooring C ended in August 2007.

A mixing length framework is employed as described by *Cole et al.* [2015]. The mixing length, λ, and horizontal diffusivity, K_λ, are estimated as:

$$\lambda = \frac{\overline{\theta'_{iso}\theta'_{iso}}^{1/2}}{|\nabla\overline{\theta}_{iso}|} \tag{6}$$

$$K_\lambda = c_0 \lambda \overline{u'u'}^{1/2}, \tag{7}$$

where θ_{iso} is the temperature along a density surface, u the horizontal velocity vector, and c_0 a mixing efficiency [*Tennekes*, 1972; *Armi and Stommel*, 1983; *Naveira Garabato et al.*, 2011; *Abernathey and Cessi*, 2014]. The mixing efficiency is taken to be $c_0 = 0.16$ [*Wunsch*, 1999; *Klocker and Abernathey*, 2014]. Primed quantities denote a fluctuation from the mean; temperature and velocity were first averaged with a 30-day timescale, and then all variability at timescales larger than one year was removed. The timescales are chosen to exclude higher

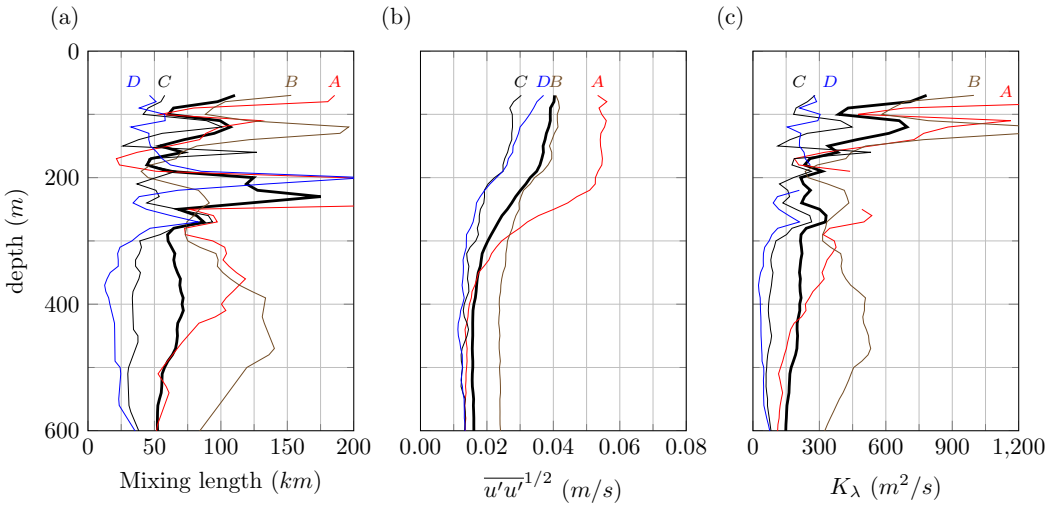

Figure 4. Profiles of a) mixing length, b) magnitude of velocity fluctuations, and c) along-isopycnal eddy diffusivity K_λ at the four BGOS moorings. The black thick line denotes the mean among the four moorings. Extraneous mixing lengths at moorings A and D (red and blue) over 200-250 m depth are excluded from the diffusivity calculation (see text).

frequency variability primarily in the velocity observations, and to represent the mesoscale dynamics of the system. Overbar denotes a temporal average over all years. The spatial gradient of the mean temperature field, $\nabla\overline{\theta}_{iso}$, is estimated along density surfaces from MIMOC [*Schmidtko et al.*, 2013] at a 100 km scale. The calculation is performed independently on each density surface and for each mooring. Only the upper 600 m are presented here.

The mixing length framework assumes that temperature and salinity anomalies along a density surface are determined by horizontal processes, and that vertical processes are negligible. Two of the moorings, *A* and *D*, fail this criteria in the 200-250 m depth range where horizontal gradients are very small; these regions lead to an elevated mixing length (Figure 4a), and are excluded from the horizontal diffusivity estimate (Figure 4c).

A range of mixing lengths, velocity fluctuations, and diffusivities were found at the four moorings (Figure 4). Mixing length values ranged from less than 50 to near 200 km. Velocity fluctuations decayed by more than a factor of two between 70 m and 300 m depth, and then remained constant at approximately 0.02 m s^{-1}. Both mixing length and velocity fluctuations are small in comparison to other regions [*Cole et al.*, 2015]. Eddy diffusivities ranged from 100 to more than 600 m^2 s^{-1}, with a factor of two decay with depth from 70 to 300 m arising from that of the velocity fluctuations. There was significant variability in all quantities between the moorings, with mooring B having elevated mixing lengths, velocity fluctuations, and diffusivity at all depths due to its proximity to the basin boundary and the Chukchi Plateau, a source of eddies that transit past mooring B [*Carpenter and Timmermans*, 2012].

There are considerable uncertainties in our evaluation of K_λ. The mixing length is not always well conditioned, as seen for example for moorings A and D. Eddy kinetic energy depends on the period over which the cutoff is applied; here we have chosen 30 days, but higher EKE is obtained for higher frequency cutoffs. As an example, a 7 days cutoff (which would capture more eddies) results in an approximately 30% larger EKE and eddy diffusivity. The value of c_0, here set to 0.16, depends on the decorrelation timescale of the eddies which could very well be different in the Arctic from elsewhere. Nevertheless, despite the

uncertainties in our estimates of K_λ and K_D, they are broadly similar to one-another both in magnitude and in their vertical structure.

5 Discussion and implications

Guided by residual mean theory and the observed structure of the halocline in the BG, we have mapped out the magnitude and spatial pattern of eddy diffusivity required to exactly balance the Eulerian-mean flow set up by winds (Ekman processes mediated by ice) blowing over the surface. We find eddy diffusivities K_D that vary from order $400\,\mathrm{m^2\,s^{-1}}$ at the surface decaying rapidly over the halocline to order $50\,\mathrm{m^2\,s^{-1}}$ at a depth of 300 m or so, and close to the center of the gyre. We remark that both the eddy diffusivity value and its spatial structure are in broad agreement with results from eddy resolving numerical simulation by *Manucharyan et al.* [2016] (see Figure 3 of that paper).

Estimates of eddy diffusivity K_λ, employing mixing length theory based on BG mooring measurements, are at least as large as K_D, with broadly the same vertical structure. Despite the significant uncertainties in both estimates of K_λ and K_D outlined at the end of §3 and §4, our results indicate that the eddy-induced transport in the BG is of the same order of magnitude as that required to balance the accumulation of freshwater by Ekman pumping, estimated using an ocean surface stress climatology.

This suggests that the residual flow is small in the halocline of the Beaufort Gyre, and has the following implications:

1. freshwater, heat and tracer transport in the BG, which is achieved by the residual flow, is likely very different from that based on the Eulerian mean circulation, the quantity conventionally mapped from observations.
2. the small residual overturning circulation implies a scaling $H \simeq \frac{R\tau}{\rho_0 f_0 K_D}$ for the depth of the halocline (from Eq.4 where R is the radius of the gyre. This is the scaling for the depth of the thermocline in the ACC postulated by *Marshall and Radko* [2003] and the depth of the halocline found by *Manucharyan et al.* [2016] and *Manucharyan and Spall* [2016] in their idealized models of the BG.
3. models of the Arctic require a mesoscale parameterization with diffusivities around $500\,\mathrm{m^2\,s^{-1}}$ decaying over the depth of the halocline to small values in the abyss.
4. how models respond to a change in the wind may be dependent on how they parameterize mesoscale eddies, since eddies play a zero-order role in mediating the freshwater budget of the gyre.

Finally, it should be said that the present analysis is not exhaustive, and other mechanisms may influence the BG dynamics. Several processes may contribute to setting or modifying the observed Ekman pumping rate, e.g., vertical mixing of halocline waters or upwelling in winter driven by the interaction of the geostrophic current with winter fast ice. The analysis of the relative importance of such seasonal upwelling versus eddy diffusivity in deflating the gyre is the subject of a follow up paper. Regardless of the specific mechanisms that may contribute to the annually averaged Ekman pumping rate, eddy bolus fluxes are capable of balancing this observed Ekman pumping. Future work should additionally attempt to more precisely constrain the estimates presented here. One possibility would be to carry out a tracer release in the halocline of the BG following the example of the DIMES experiment [*Gille et al.*, 2012] in the Southern Ocean. The rates of lateral and vertical dispersion can then yield direct information about mesoscale eddy stirring rates and diapycnal mixing rates.

Acknowledgments

We thank Jean-Michel Campin, Edward Dorridge, Andrey Proshutinsky and Miles McPhee for their help and insights. The experiments described here were made possible by support from the NSF program in Arctic Research, Award Number 1603557. STC was supported through NSF award numbers 1355668 and 1602926.

NCEP Reanalysis data provided by the NOAA/OAR/ESRL PSD, Boulder, Colorado, USA, from their Web site at `http://www.esrl.noaa.gov/psd/` [*Kalnay et al.*, 1996]

Arctic dynamic topography data were provided by the Centre for Polar Observation and Modelling, University College London `www.cpom.ucl.ac.uk/dynamic_topography` [*Armitage et al.*, 2016]

BG mooring data were collected and made available by the Beaufort Gyre Exploration Program based at the Woods Hole Oceanographic Institution (`http://www.whoi.edu/beaufortgyre`) in collaboration with researchers from Fisheries and Oceans Canada at the Institute of Ocean Sciences. Data are online at: http://www.whoi.edu/website/beaufortgyre/data.

All data for this paper is properly cited and referred to in the reference list.

References

Abernathey, R., and P. Cessi (2014), Topographic Enhancement of Eddy Efficiency in Baroclinic Equilibration, *Journal of Physical Oceanography*, *44*(8), 2107–2126, doi:10.1175/JPO-D-14-0014.1.

Andrews, D. G., and M. E. McIntyre (1976), Planetary Waves in Horizontal and Vertical Shear: The Generalized Eliassen-Palm Relation and the Mean Zonal Acceleration, *Journal of the Atmospheric Sciences*, *33*, 2031–2048, doi:10.1175/1520-0469(1976)033<2031:PWIHAV>2.0.CO;2.

Armi, L., and H. Stommel (1983), Four Views of a Portion of the North Atlantic Subtropical Gyre, *Journal of Physical Oceanography*, *13*(5), 828–857, doi:10.1175/1520-0485(1983)013<0828:FVOAPO>2.0.CO;2.

Armitage, T. W. K., S. Bacon, A. L. Ridout, S. F. Thomas, Y. Aksenov, and D. J. Wingham (2016), Arctic sea surface height variability and change from satellite radar altimetry and GRACE, 2003-2014, *Journal of Geophysical Research: Oceans*, *121*(6), 4303–4322, doi:10.1002/2015JC011579.

Armitage, T. W. K., S. Bacon, A. L. Ridout, A. A. Petty, S. Wolbach, and M. Tsamados (2017), Arctic Ocean geostrophic circulation 2003-2014, *The Cryosphere Discussions*, *2017*, 1–32, doi:10.5194/tc-2017-22.

Carpenter, J. R., and M.-L. Timmermans (2012), Deep mesoscale eddies in the Canada Basin, Arctic Ocean, *Geophysical Research Letters*, *39*(20), 1–6, doi:10.1029/2012GL053025.

Cavalieri, D. J., C. L. Parkinson, P. Gloersen, and H. J. Zwally (1996), Sea Ice Concentrations from Nimbus-7 SMMR and DMSP SSM/I-SSMIS Passive Microwave Data, Version 1, doi:10.5067/8GQ8LZQVL0VL.

Cole, S. T., C. Wortham, E. Kunze, and W. B. Owens (2015), Eddy stirring and horizontal diffusivity from Argo float observations: Geographic and depth variability, *Geophysical Research Letters*, *42*(10), 3989–3997, doi:10.1002/2015GL063827.

Cole, S. T., J. M. Toole, R. Lele, M. L. Timmermans, S. G. Gallaher, T. P. Stanton, W. J. Shaw, B. Hwang, T. Maksym, J. P. Wilkinson, M. Ortiz, H. Graber, L. Rainville, A. A. Petty, S. L. Farrel, J. A. Richter-Menge, and C. Haas (2017), Ice and ocean velocity in the Arctic marginal ice zone: Ice roughness and momentum transfer, *Elementa: Science of the Anthropocene, in press*, doi:10.1525/elementa.241.

Danabasoglu, G., J. C. Mcwilliams, and W. G. Large (1996), Approach to equilibrium in accelerated global oceanic models, *Journal of Climate*, *9*(5), 1092–1110, doi:10.1175/1520-

0442(1996)009<1092:ATEIAG>2.0.CO;2.

Gille, S., J. R. Ledwell, A. C. Naveira Garabato, K. Speer, D. Balwada, A. Brearley, J. B. Girton, A. Griesel, R. Ferrari, A. Klocker, J. H. LaCasce, P. Lazarevich, N. Mackay, M. P. Meredith, M.-J. Messias, B. Owens, J.-B. Sallée, K. Sheen, E. Shuckburgh, D. A. Smeed, L. C. St.Laurent, J. M. Toole, A. J. Watson, N. Wienders, and U. Zajaczkovski (2012), The Diapycnal and Isopycnal Mixing Experiment: A First Assessment, *J. Phys. Oceanogr.*, *17*(58), 2009–2011, doi:10.1029/2009JC005821.CLIVAR.

Kalnay, E., M. Kanamitsu, R. Kistler, W. Collins, D. Deaven, L. Gandin, M. Iredell, S. Saha, G. White, J. Woollen, Y. Zhu, M. Chelliah, W. Ebisuzaki, W. Higgins, J. Janowiak, K. C. Mo, C. Ropelewski, J. Wang, A. Leetmaa, R. Reynolds, R. Jenne, and D. Joseph (1996), The NCEP/NCAR 40-year reanalysis project, *Bulletin of the American Meteorological Society*, *77*(3), 437–471, doi:10.1175/1520-0477(1996)077<0437:TNYRP>2.0.CO;2.

Klocker, A., and R. Abernathey (2014), Global Patterns of Mesoscale Eddy Properties and Diffusivities, *Journal of Physical Oceanography*, *44*(3), 1030–1046, doi:10.1175/JPO-D-13-0159.1.

Locarnini, R. A., A. V. Mishonov, J. I. Antonov, T. P. Boyer, H. E. Garcia, O. K. Baranova, M. M. Zweng, C. R. Paver, J. R. Reagan, D. R. Johnson, M. Hamilton, and D. Seidov (2013), World Ocean Atlas 2013. Vol. 1: Temperature., *Tech. Rep. September*, doi:10.1182/blood-2011-06-357442.

Lu, P., Z. Li, B. Cheng, and M. Leppäranta (2011), A parameterization of the ice-ocean drag coefficient, *Journal of Geophysical Research*, *116*(C7), C07,019, doi:10.1029/2010JC006878.

Manley, T. O., and K. Hunkins (1985), Mesoscale Eddies of the Arctic Ocean, *Journal of Geophysical Research C Oceans*, *90*(C3), 19, doi:10.1029/JC090iC03p04911.

Manucharyan, G. E., and M. A. Spall (2016), Wind-driven freshwater buildup and release in the Beaufort Gyre constrained by mesoscale eddies, *Geophysical Research Letters*, doi:10.1002/2015GL065957.

Manucharyan, G. E., M. A. Spall, and A. F. Thompson (2016), A Theory of the Wind-Driven Beaufort Gyre Variability, *Journal of Physical Oceanography*, (2013), 3263–3278, doi:10.1175/JPO-D-16-0091.1.

Marshall, J., and T. Radko (2003), Residual-Mean Solutions for the Antarctic Circumpolar Current and Its Associated Overturning Circulation, *Journal of Physical Oceanography*, *33*(11), 2341–2354, doi:10.1175/1520-0485(2003)033<2341:RSFTAC>2.0.CO;2.

Marshall, J., and K. Speer (2012), Closure of the meridional overturning circulation through Southern Ocean upwelling, *Nature Geoscience*, *5*(3), 171–180, doi:10.1038/ngeo1391.

McPhee, M. G. (2013), Intensification of geostrophic currents in the Canada Basin, Arctic Ocean, *Journal of Climate*, *26*(10), 3130–3138, doi:10.1175/JCLI-D-12-00289.1.

Naveira Garabato, A. C., R. Ferrari, and K. L. Polzin (2011), Eddy stirring in the Southern Ocean, *Journal of Geophysical Research: Oceans*, *116*(9), doi:10.1029/2010JC006818.

Nurser, A. J. G., and S. Bacon (2014), The rossby radius in the arctic ocean, *Ocean Science*, *10*(6), 967–975, doi:10.5194/os-10-967-2014.

Plumb, R. A., and R. Ferrari (2005), Transformed Eulerian-Mean Theory. Part I: Nonquasi-geostrophic Theory for Eddies on a Zonal-Mean Flow, *Journal of Physical Oceanography*, *35*(2), 165–174, doi:10.1175/JPO-2669.1.

Proshutinsky, A., R. Krishfield, M.-l. Timmermans, J. Toole, E. Carmack, F. Mclaughlin, W. J. Williams, S. Zimmermann, M. Itoh, and K. Shimada (2009), Beaufort Gyre freshwater reservoir : State and variability from observations, *Journal of Geophysical Research*, *114*, 1–25, doi:10.1029/2008JC005104.

Proshutinsky, A., D. Dukhovskoy, M.-l. Timmermans, R. Krishfield, and J. L. Bamber (2015), Arctic circulation regimes, *Philosophical transactions. Series A, Mathematical, physical, and engineering sciences*, *373*(2052), 20140,160, doi:10.1098/rsta.2014.0160.

Proshutinsky, A. Y., and M. A. Johnson (1997), Two circulation regimes of the wind-driven Arctic Ocean, *Journal of Geophysical Research: Oceans*, *102*(C6), 12,493–12,514, doi:10.1029/97JC00738.

Schmidtko, S., G. C. Johnson, and J. M. Lyman (2013), MIMOC: A global monthly isopycnal upper-ocean climatology with mixed layers, *Journal of Geophysical Research: Oceans*, *118*(4), 1658–1672, doi:10.1002/jgrc.20122.

Tennekes, H. (1972), *A First Course in Turbulence*, 300 pp., doi:10.1017/S002211207321251X.

Timmermans, M.-L., J. Toole, A. Proshutinsky, R. Krishfield, and A. Plueddemann (2008), Eddies in the Canada Basin, Arctic Ocean, Observed from Ice-Tethered Profilers, *Journal of Physical Oceanography*, *38*(1), 133–145, doi:10.1175/2007JPO3782.1.

Tschudi, M., C. Fowler, J. S. Maslanik, and W. Meier (2016), Polar Pathfinder Daily 25 km EASE-Grid Sea Ice Motion Vectors, Version 3., doi:10.5067/O57VAIT2AYYY.

Wunsch, C. (1999), Where do ocean eddy heat fluxes matter?, *Journal of Geophysical Research: Oceans*, *104*(C6), 13,235–13,249, doi:10.1029/1999JC900062.

Yang, J. (2006), The seasonal variability of the Arctic Ocean Ekman transport and its role in the mixed layer heat and salt fluxes, *Journal of Climate*, *19*(20), 5366–5387, doi:10.1175/JCLI3892.1.

Yang, J. (2009), Seasonal and interannual variability of downwelling in the Beaufort Sea, *J Geophys Res*, *114*, C00A14, doi:10.1029/2008JC005084.

Zhao, M., M. L. Timmermans, S. Cole, R. Krishfield, A. Proshutinsky, and J. Toole (2014), Characterizing the eddy field in the Arctic Ocean halocline, *Journal of Geophysical Research C: Oceans*, *119*(12), 8800–8817, doi:10.1002/2014JC010488.

Zhao, M., M. L. Timmermans, S. Cole, R. Krishfield, and J. Toole (2016), Evolution of the eddy field in the Arctic Ocean's Canada Basin, 2005-2015, *Geophysical Research Letters*, *43*(15), 8106–8114, doi:10.1002/2016GL069671.

Zweng, M. M., J. Reagan, J. Antonov, A. Mishonov, T. Boyer, H. Garcia, O. Baranova, D. Johnson, D. Seidov, and M. Bidlle (2013), World Ocean Atlas 2013, Volume 2: Salinity, *Tech. Rep. 1*, doi:10.1182/blood-2011-06-357442.